Process-Microstructure-Property Relationship in the Directed Energy Deposition of

Cobalt-Chromium Alloy (Stellite 21) Coatings

Ziyad Smoqi^a, Joshua Toddy^b, Harold (Scott) Halliday^b, Jeffrey E. Shield^a, Prahalada Rao^{a*}

(a) Mechanical and Materials Engineering, University of Nebraska-Lincoln

(b) Center for Advanced Manufacturing, Navajo Technical University

* corresponding author, email: rao@unl.edu

Abstract

In this work, we accomplished the crack-free directed energy deposition (DED) of a multi-

layer Cobalt-Chromium alloy coating (Stellite 21) on Inconel 718 substrate. Stellite alloys are used

as coating materials given their resistance to wear, corrosion, and high temperature. The main

challenge in DED of Stellite coatings is the proclivity for crack formation during printing. The

objective of this work is to characterize the effect of the laser power and localized laser-based

preheating on the physical properties of the deposited coating, namely, crack formation,

microstructural evolution, dilution of the coating composition due to diffusion of iron and nickel

from the substrate, and microhardness. It is observed that cracking is alleviated on preheating the

substrate and depositing the coating at a moderate input energy (laser power) level. The main

finding is that cracking of DED-processed Stellite 21 coating is linked to the segregation of brittle

chromium and molybdenum phases at the inter-dendritic regions. Localized laser-based preheating

and moderate laser power mitigate steep temperature gradients and thereby avoid thermally-

induced cracking of the Stellite coating along the inter-dendritic regions.

Keywords: Additive manufacturing; Directed energy deposition; Stellite coating;

Microstructure; Cracking; Microhardness;

1

1 Introduction

Stellite alloys (a tradename of Kennametal) are used as corrosion-, wear-, and temperature-resistant coatings on automotive valve seating surfaces, cutting tools, gun barrels, steam turbines, among others [1-4]. A recent trend is to use powder-based directed energy deposition (DED) additive manufacturing to deposit Stellite coatings [5-7]. In the DED process, illustrated in Figure 1, material in the form of powder is sprayed onto a substrate through nozzles and fused (melted) using a laser. The part is built in three dimensions by relative movement of the nozzle and part [8].

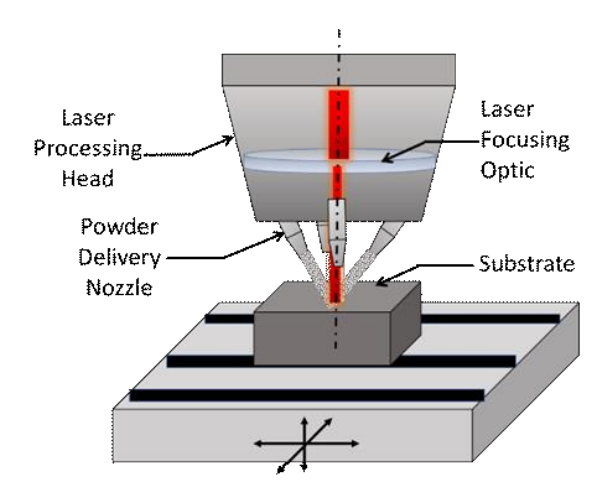


Figure 1: Schematic of the DED process. Metal powder is sprayed from the sides and fused by using energy from a laser beam.

DED is an attractive approach for depositing Stellite coatings compared to weld overlay-based coatings because the microstructure evolved is finer and has higher hardness [9-12]. In both DED and welding the coating forms a metallurgical bond with the substrate. Consequently, the coating and the substrate intermix, which tends to reduce the hardness, wear and corrosion resistance of the coating [13]. However, in the case of DED the intermixing is limited [10, 11]. Despite these advantages, the main challenge in DED of Stellite coatings is the propensity for crack formation [10, 14]. Hence, if crack-free deposition of Stellite coatings can be realized using DED, it will substantially improve the life of engineering components.

Accordingly, the objective of this work in the context of DED of a specific grade of Stellite (Stellite 21) coatings on Inconel 718 substrate is to explain and quantify the effect of input energy (laser power) used for deposition and preheating of the substrate on crack formation, microstructural evolution, dilution and the microhardness of the coating. Preheating was achieved by traversing the laser on the substrate prior to deposition, termed localized laser-based preheating [14, 15]. Realizing this objective results in the identification of a suitable process window for crack-free deposition of Stellite 21 coatings. Furthermore, we correlate the temperature trends symptomatic of crack formation in Stellite 21 coatings by acquiring in-situ temperature signatures using thermocouples.

In summarizing the literature, we note that while the effect of process conditions, including preheating, on the microstructure evolved of DED-processed Stellite 6 coatings have been extensively studied compared to fewer studies for Stellite 21 [7, 15]. Stellite 6 contains tungsten (~4.5 wt.%) as an alloying element, whereas in Stellite 21, tungsten is replaced by molybdenum. Furthermore, Stellite 6 has a higher carbon content (> 0.8%, compared to < 0.4% for Stellite 21) [16]. Compared to Stellite 6, Stellite 21 is more resistant to corrosion and creep [17-20].

The link between formation of Cr- and Mo-rich inter-dendritic regions and crack formation in Stellite 21 is demonstrated in the work of Ganesh *et al.* [15] who investigated the fracture behavior of laser-clad Stellite 21 on AISI 316L stainless steel. They correlated the occurrence of brittle inter-dendritic fracture with the formation of columnar dendrites with Cr- and Mo- rich fine carbide phases in the inter-dendritic region. These brittle carbide phases in the inter-dendritic region of Stellite 21 clad provided low energy paths for crack propagation under tensile loading [15].

Recently, Traxel and Bandopadhyay [5] demonstrated the DED of Stellite 6 coatings on tool steel coupons. In some of their samples, they also remelted the top layer of the coating by an

additional pass by the laser. An important finding by Bandopadhyay and Traxel is the formation of Co-rich dendritic regions and Cr-rich inter-dendritic regions in the Stellite 6 coating.

Bartkowski *et al.* [21] reported results from the microstructural analysis, and electrochemical corrosion studies of Stellite 6 coatings deposited on stainless steel coupons. Their work also demonstrated that higher laser power is linked to the increased intermixing of substrate materials into the coating which reduces the microhardness. For example, the surface microhardness of the coating increased from 550 HV_{0.5} to 680 HV_{0.5} when the laser power was increased from 400 W to 550 W; on increasing the laser power to 700 W, the microhardness decreased to 550 HV_{0.5}. Bartkowski *et al.* [21] also observed the formation of a dendritic microstructure.

Besides corroborating these previous findings, our work provides deeper understanding of the microstructure evolved by measuring the segregation of Cr- and Mo-rich phases in the interdendritic regions, as well as quantifying the degree of intermixing in substrate and coating elements using energy-dispersive X-ray spectroscopy. Additionally, we not only measure the surface microhardness of the coating, but also track the microhardness as a function of the distance of the coating from the substrate.

D'Oliveira *et al.* [22] studied the microstructural evolution and residual stresses involved in the deposition of Stellite 6 on 304 stainless steel and reported the cracking of the Stellite 6 coating surface on account of thermally-induced residual stresses. Preheating the substrate has been shown to reduce crack formation in the DED of Stellite 6 coatings [23-26]. For example, Jendrzejewski *et al.* [23] reported that a crack-free Stellite 6 coating was achieved by preheating the substrate to a temperature above 650 °C.

The effect of localized laser-based preheating of the substrate on crack formation and microstructure evolution in Stellite 1 was studied by Khajepour and co-workers [24, 26]. Through

experimental and numerical simulations, they explain that laser-based preheating of the substrates leads to relatively lower cooling rates throughout the deposition process, which in turn mitigates cracking. Furthermore, preheating the sample was correlated to a more uniform surface hardness and even distribution of a dendritic morphology. Our work provides deeper insight into the effect of preheating on crack formation by measuring penetration and density of cracks using X-ray computed tomography, and tracking temperature trends during deposition using contact-based thermocouples.

2 Materials and Methods

2.1 Materials

Powder was supplied by Oerlikon Metco and is listed under the trade name MetcoClad 21 [27], which is similar in chemistry to Kennametal's Stellite 21 powder material. Here, we refer to the material by its more popular tradename Stellite 21 [27]. The powder was produced by gas atomization and has an average particle size of 145 μ m (50 μ m standard deviation). The substrate was a 38 mm \times 38 mm \times 5.5 mm Inconel 718 alloy test coupon. The nominal chemical compositions of both the powder and substrate materials are listed in Table 1.

Table 1: The chemical Composition of MetcoClad 21 powder and as-received Inconel 718 substrate.

	Alloying Elements (wt.%)								
MetcoClad 21	Co	Cr	Mo	F	e	Ni	Mn	С	Si
Powder	Base	27.0	5.5	≤3	3.0	2.75	0.1 - 1	0.2	< 1.0
Inconel 718 Substrate	Ni Base	Cr 19	Mo 3.05	Fe 18.5	Ti 0.9	Ta 5.13	Al 0.5	C 0.04	Others B, Co, Cu, Mn, Si

2.2 Experimental Setup

Prior to deposition, the surface of the substrate was sandblasted to facilitate the adhering of the coating to the surface and to make the surface less reflective. After sandblasting the samples were cleaned with acetone to remove contaminants. A new substrate coupon was used for each experimental condition tested in this work. The test coupon was secured in a custom-built fixture; Figure 2(a) shows the fixture set up inside the machine. To prevent oxidation of the coating during DED processing, the chamber was maintained under an argon atmosphere with the oxygen concentration kept below 15 ppm.

Three contact-based K-type sheathed thermocouple probes (Omega TJ 24-CA-IN-18-G-3-CC-OSTW-M) were extended through holes drilled in the fixture. The configuration of thermocouples with respect to the Inconel 718 coupon inside the fixture is shown in Figure 2(b). The particular model of thermocouples used in this work is manufactured within a sheath of Inconel 718 to minimize errors which may be introduced if the cladding material of the thermocouple is different than the substrate.

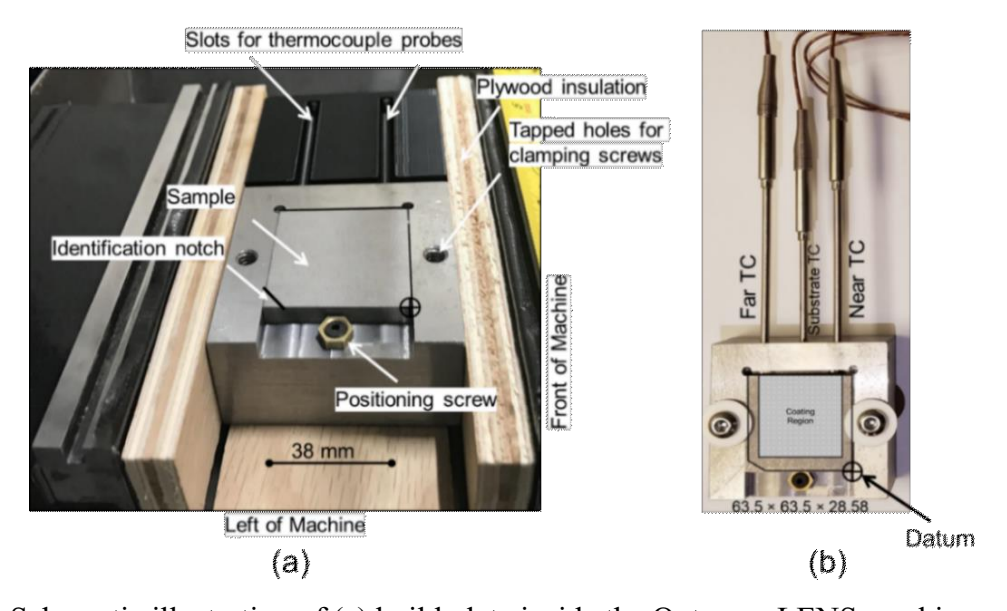


Figure 2: Schematic illustration of (a) build plate inside the Optomec LENS machine, and (b) three Inconel 718 clad K-type thermocouples used for measuring in-situ temperature.

Two thermocouples contact the sides of the substrate, and a third resides in the fixture. In Figure 2(b) the thermocouples in contact with the substrate are labeled as *Near TC* and *Far TC*, the third thermocouple inside the fixture is labeled as *Substrate TC*. The label *Near* TC demarcates that the thermocouple is nearest to the door of the machine (i.e., closest to the operator), likewise, the thermocouple farthest from the door is referred to as the *Far TC*. A hexagonal-shaped nut on the far side applies lateral clamping force against the coupon to ensure secure contact with the thermocouples. Thermally conductive paste was applied to the bottom of the coupon to ensure good contact with the substrate and eliminate air gaps. The thermocouples acquired temperature data at a rate of 50 Hz.

2.3 Experiments

Stellite 21 powder was deposited on the Inconel 718 substrate coupons using an Optomec LENS MTS 500 controlled atmosphere hybrid DED system. The powder was fed through four nozzles coaxial with a 1 kW Ytterbium infrared fiber laser (IPG) with Argon as the carrier gas. Two process parameters were varied, the preheat laser power (Ph) and deposition laser power (Pd). The process settings are summarized in Table 2.

We aggregate the processing parameters in terms of the volumetric energy density (E_v) , where $E_v = P_d/(V \cdot T \cdot H)$ [J·mm⁻³]. P_d is the deposition laser power [W], V is the translational velocity of the nozzle [mm·s⁻¹], T is the height of each layer deposited [mm], and H is the hatch spacing [mm], which is the distance between the centers of successive laser passes. The use of the volumetric energy density (E_v) facilitates the transferability and generalizability of the proposed parameter window to other DED systems.

Table 2: Fixed and varied process parameters used in DED of Stellite 21 on Inconel 718.

Process Step	Laser Power	Deposition Pattern	Scan Velocity	Hatch Spacing	Layer Thickness
Preheat (2 layers)	P [W] Varied at 4 levels $P_h = 0, 300, 350,$ 400	Rectilinear, 0.70 mm distance between hatches	V[mm/s] 5.1	H [mm] 0.7 (= laser spot size (d))	T [mm] N/A
Deposition (12 layers)	Varied at 4 levels $P_d = 200, 225, 250, 275$	Rectilinear, 95% overlap between hatches	10.6	0.375 (1.5 × T)	0.25

Figure 3 shows the experimental schema for preheat and deposition . During the preheat and deposition processes, the substrate translates in the X-Y directions as shown in Figure 3(a), while the deposition head traveled in the positive Z-direction at the end of each layer. The substrate was preheated by scanning the laser in a rectilinear pattern, as shown in Figure 3(b). Three different laser power settings were used for preheating (P_h = 300, 350, 400 W), and control samples were deposited without preheating (P_h = 0).

For the preheating passes, the laser scans starts with a counterclockwise contour from bottom left corner in Figure 3(b)) and follows a rectilinear pattern with no overlap between adjacent passes (tracks). The scanning velocity for preheating was set at 5.1 mm·s⁻¹. Two identical passes of preheating were conducted starting and ending at the same point with the laser turned off at the end of each pass during the process. The aforementioned range of laser power for preheating was selected through initial tests. The coupons warped excessively when the preheat laser power (Ph) was in excess of 400 W; hence this value was set as the upper limit.

The deposition process was carried out at four laser powers (P_d), 200 W, 225 W, 250 W, and 275 W as shown in Figure 3(c) and (d). The machine manufacturer's recommendation is to set the layer height at T = 0.25 mm, and the hatch spacing H = 1.5 × T = 0.375 mm, resulting in a 95% overlap between adjacent passes. The distance between the tip of the laser processing head and the

substrate (stand-off distance) was 7.5 mm and the spot size of the laser was fixed at 0.7 mm (diameter). There are several factors in DED, such as the volumetric flow rate of the powder, the distance between the nozzle and substrate (standoff distance), dwell time between successive layers, deposition pattern, among others, that determine the thermal profile, and consequently, the coating characteristics. These are outside the scope of the present work.

The experimental plan used in this work is shown in Figure 4. After each test, the as-deposited coating was examined using optical microscopy; if the coating surface had visible cracks further processing in the region (direction) of the process variable was avoided. The settings of laser power and scan velocity were selected by consulting the literature. The laser power tested in this work results in volumetric energy densities ranging from 200 to 277 J·mm⁻³, the upper limit of which is close to the energy density (300 J·mm⁻³) reported by Traxel and Bandopahyay for cladding Stellite 6 onto tool steel [5].

The range of energy density used in this work also agrees with a different study by Singh *et al.* [28] on coating Stellite 6 on Steel. Singh *et al.* reported that an area-based energy density ranging from 32 J·mm⁻² to 52 J·mm⁻² resulted in a coating microhardness (HV₁₀₀) of 550 to 700. We note that the areal energy density in Singh *et al.*'s work is defined as $E_a = P_d/(V \cdot d)$, where d is the laser spot size (= 0.7 mm), With deposition powers used in our work, the corresponding energy density ranges from 27 J·mm⁻² to 37 J·mm⁻² for $P_d = 200$ W and $P_d = 275$ W, respectively.

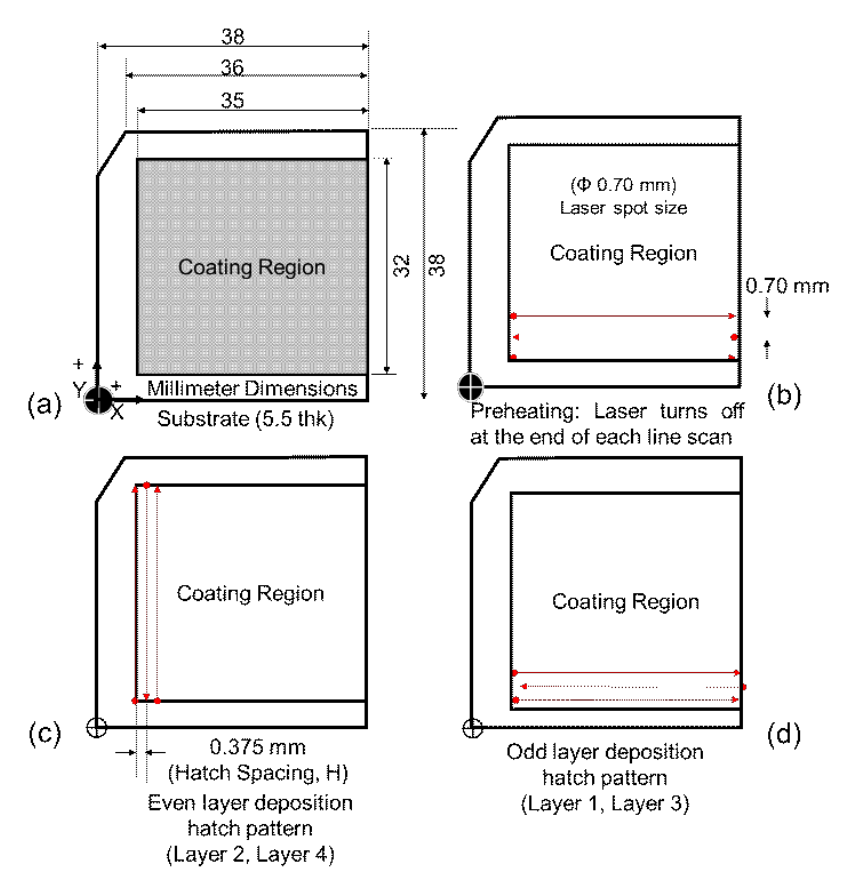


Figure 3: Experimental setup and schematic of the coupon (substrate) used for deposition. (a) dimensions of the substrate, and the coating region (b) scanning pattern for preheating. (c) and (d) scanning pattern for the deposition, which follows a 90-0° alternating hatch pattern with overlap between adjacent passes. A separate coupon is used for each experimental treatment condition.

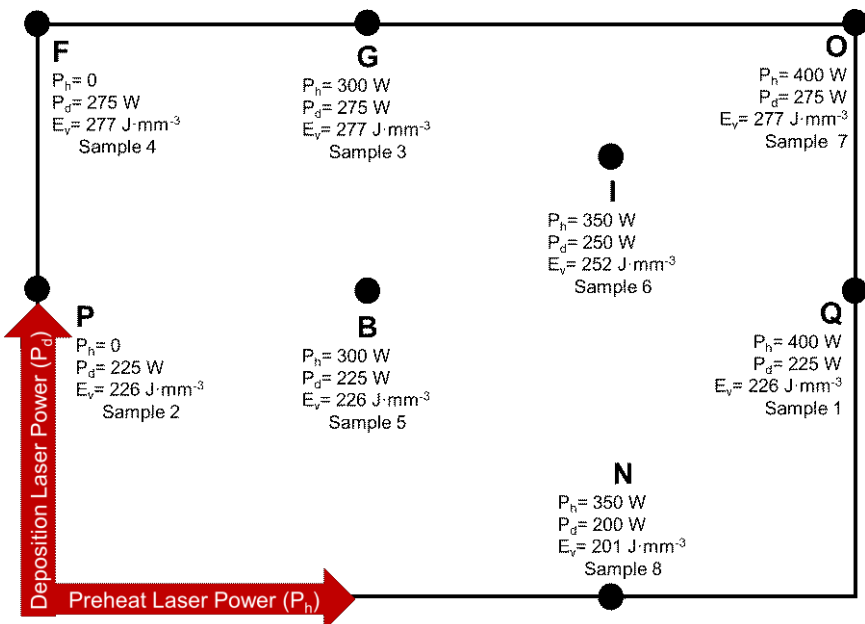


Figure 4 The experimental test plan used in conducting the experiments.

The energy density values chosen for this work also match closely with those suggested by Xu *et al.* [11], who recommended a maximum linear energy density $E_1 = P_d/V$ value of 300 J·mm⁻¹ for cladding of Stellite 6 on stainless steel. The linear energy density used in this work ranges from 188 to 260 J·mm⁻¹. The scanning speed (10.6 mm·s⁻¹) and powder flow rate (0.03 g·s⁻¹) were maintained constant throughout the experiments; the powder flow rate is the minimum possible by the machine. The mass flow rate exceeds the calculated minimum theoretical mass flow rate of 0.008 g·s⁻¹, estimated as V·T·H· ρ , where ρ is the mass density of Stellite 21 (8.33 × 10⁻³ g·mm⁻³). The large factor of safety applied to the mass flow rate ensures that there are no lack-of-fill defects. The approximate deposition time for each sample was 60 minutes; 15 additional minutes needed for samples that were preheated.

2.4 Sample Characterization

For microstructural characterization, small samples ($10 \text{ mm} \times 10 \text{ mm} \times 6.5 \text{ mm}$) were cut by wire electro-discharge machining along the cross-section of the Stellite 21 coating. Samples were mechanically ground using progressively finer grit SiC sandpaper (400, 600, 800, and 1200 grit) and polished using diamond paste ($3 \mu m$, $1 \mu m$, and $0.5 \mu m$). Finally, the samples were etched with aqua regia (hydrochloric acid-to-nitric acid was 3:1 by volume). The coating was analyzed using scanning electron (SEM), optical microscopy, and X-ray computed tomography (XCT).

Microhardness measurements (Vickers, Hv) were performed on polished surfaces under a load of 500 g and dwell time of 10 seconds, and along the coating cross-section under a load of 100 g and dwell time of 15 seconds using a Tukon 2500 Hardness Tester. Microhardness testing was performed in accordance with ASTM E384. A distance of at least 3 times the pyramidal diagonal of the Vickers indenter was maintained between a crack and location of micro indentation to avoid the effect of the cracks on the microhardness measurements.

The microstructure of the coating was characterized by a dual-beam SEM workstation (Helios 660 NanoLab, FEI). The microstructural composition was analyzed by Energy Dispersive X-ray Spectroscopy (EDS) (Octane Super, EDAX) integrated with the Helios 660. The crack density as a function of depth below the coating surface was analyzed using XCT (NorthStar Imaging) prior to polishing and etching.

3 Results and Discussion

3.1 Process-induced Cracking and Warping

3.1.1 Surface Cracking

Figure 5 shows the SEM micrographs of as-deposited coating surfaces. Cracking is exacerbated at high deposition power (P_d). This is exemplified by comparing samples F (P_h =0 W; P_d =275 W) and sample P (P_h =0 W; P_d =225 W). The highest density of cracks was observed in the coating deposited at the extreme laser power (P_d =275 W), regardless of whether the substrate was preheated. A noticeable reduction in the number of cracks was observed between sample P (P_h =0 W; P_d =225 W) and sample Q (P_h =400 W; P_d =225 W) which implies that preheating of the substrate mitigates cracking. However, it was observed that a preheat power of 400 W caused the substrate to warp. The reduction of preheating power, exemplified in Sample B (P_h =300W P_d =225W), led to a further reduction in surface cracks compared to sample Q.

The crack density under different processing conditions is quantified in Figure 6. The crack density (η) is determined from the SEM images as $\eta = \frac{8}{\pi^3} M l^2$, where M is the total number of cracks per unit area in an SEM image, and l the average length of the cracks [29]. Crack density was measured from 38 SEM images of dimensions ~ 2 mm × 2 mm.

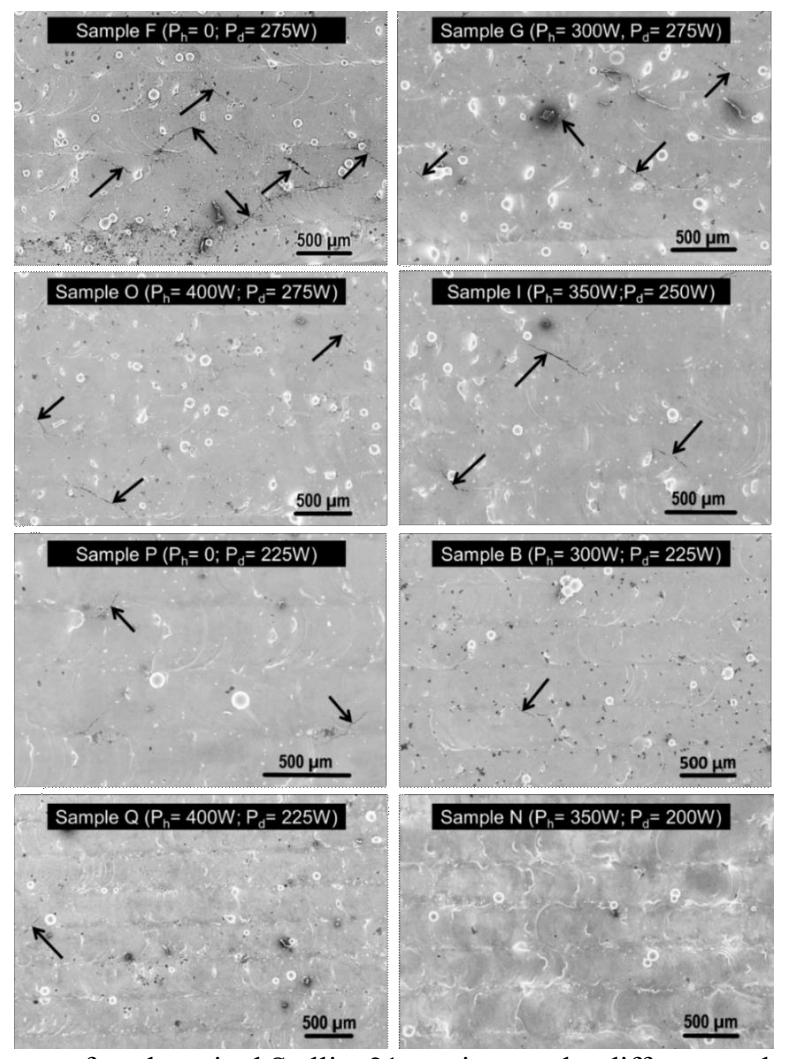


Figure 5: SEM images of as-deposited Stellite 21 coatings under different preheat and deposition power settings. Arrows indicate cracks.

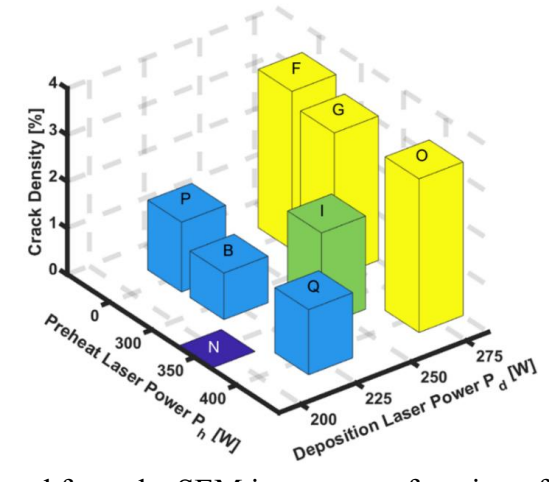


Figure 6: Crack density extracted from the SEM images as a function of preheating and deposition laser powers. Crack density was measured from 38 SEM images of dimensions \sim 2 mm \times 2 mm.

3.1.2 Crack Depth

Figure 7 shows the optical micrographs of surface, longitudinal and transverse cross-sections for five samples, namely, F, O, P, Q, and N after polishing and etching. Longitudinal cross-sections are made parallel to the scan direction of the first deposited layer; transverse cross-sections are perpendicular to the scan direction of the first layer. A prominent inference from Figure 7 is that the crack density decreases significantly when the substrate is preheated and the laser power for deposition is reduced to a moderate or low level.

From Figure 7, we observe that samples deposited at relatively higher laser power, such as samples F (P_d = 275 W, P_h = 0 W) and O (P_d = 275 W, P_h = 400 W) have prominent cracks. For instance, in the case of sample F, which is not preheated (P_h = 0), and the coating is deposited at the highest power setting (P_d = 275 W); the depth of a representative crack is ~350 μ m. Moreover, on comparing sample P (P_d = 225 W, P_h = 0 W) and Q (P_d = 225 W, P_h = 400 W) it is evident that the crack density decreases significantly when the substrate is preheated and the laser power for deposition is reduced to a moderate level.

In the transverse cross-section micrographs in Figure 7, it is observed that those samples (O, Q, and N) whose substrates have been preheated show troughs and peaks corresponding to passes made by the laser during preheating. The presence of troughs and peaks, demarcated as A in Figure 7, indicates that the material was melted during preheating. The melting of the substrate implies that the local temperature exceeds 1250 °C, viz., the lower bound of the melting temperature for Inconel 718. Peaks and troughs, indicative of remelting of the substrate, were also observed in samples which were not preheated but were processed at high deposition power, such as sample

F. However, the remelting depth of the substrate in sample F was measured to be in the range of 50 μm and is not as prominent as in Sample O.

A consequential observation in Figure 7 is that cracking is restricted to only the topmost layers and not near the substrate; both longitudinal and transverse cross-sections confirm that the cracks do not extend beyond 350 µm in the worst-case scenario (sample F). More pertinently, no cracks were evident in the interface region, which implies a strong bonding between the substrate and coating. An explanation for the observation that cracks are only present in the topmost layers is tendered as follows. Cracks are initiated from the layer being currently processed and propagate towards the interface. However, when the next layer is deposited on top, the layers at the bottom are re-melted, and the molten material from remelting heals the cracks.

The remelting of material is advantageous from a practical perspective; if cracking is detected in a timely manner using in-situ sensors they can be readily corrected by making an additional pass by the laser, which will remelt and heal (refill) the cracks. The remelting of layers at the bottom was also reported by Sun *et al* [30]. To substantiate these observations, we examine the morphology and depth of the cracks using XCT analysis.

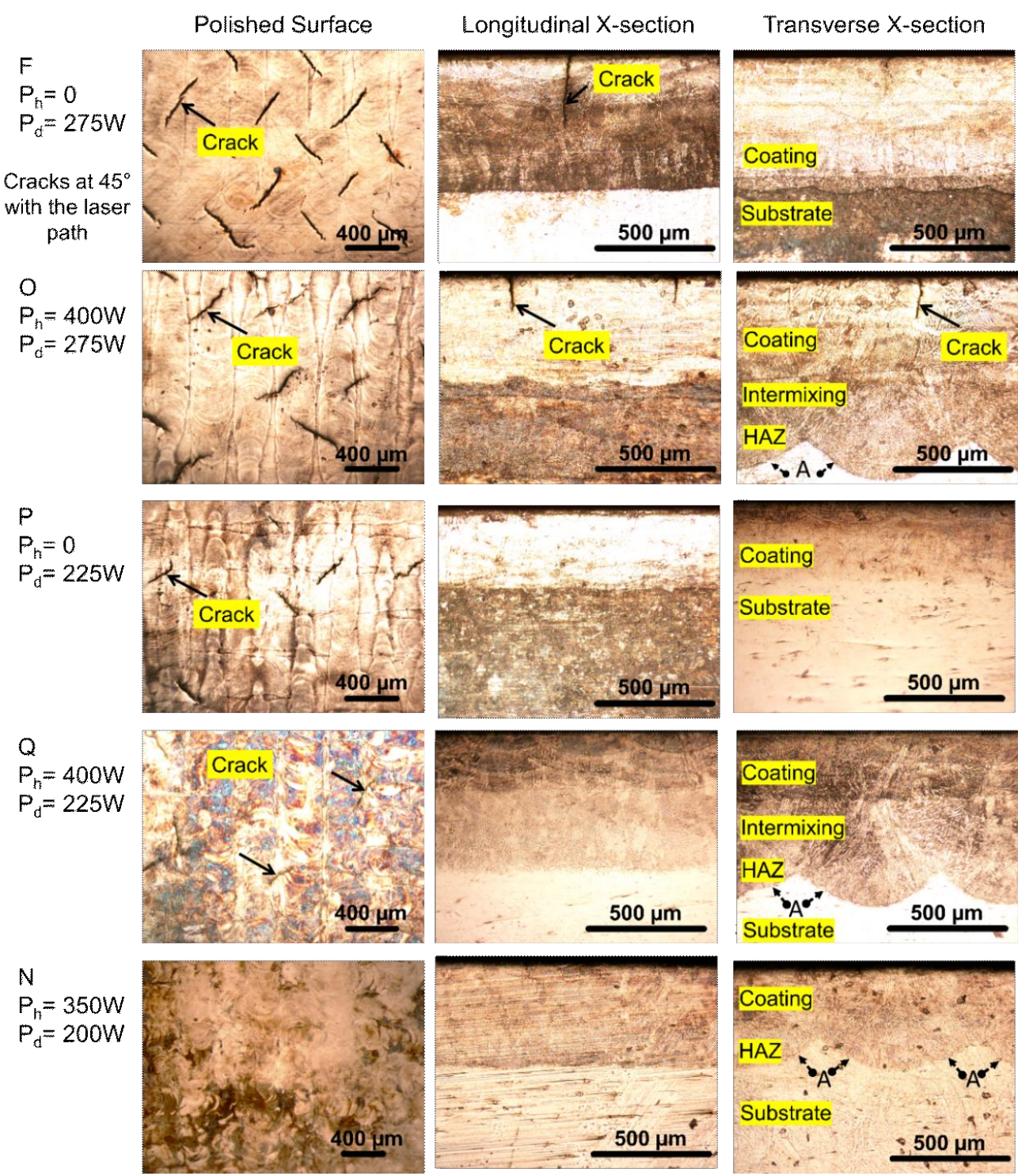


Figure 7: Optical micrographs of the etched and polished surfaces, longitudinal and transverse cross-sections of Stellite 21 coating under different preheat and deposition power settings.

The crack density as a function of depth below the coating surface was ascertained through XCT scanning. Figure 8 shows the XCT of two representative samples at voxel size of 15 μ m, F ($P_h = 0$ W, $P_d = 275$ W) and G ($P_h = 300$ W, $P_d = 275$ W) at similar locations beneath the surface of as-deposited coatings. We observe that at depth of 300 - 350 μ m from the top surface of the coating, the number of cracks was reduced by ~50% in comparison with crack density observed at depths of 150 - 300 μ m. Moreover, no cracks are evident at a depth of 350 μ m and beyond.

Thus, we conclude that the crack density decreases with depth below the surface and that the substrate-coating interface is free from cracks. This observation indicates that the cracks were initiated at the layer being deposited and propagated towards the interface. Apart from the observation that cracks are only restricted to the topmost layers, the XCT analysis attests to the observation that remelting of prior layers can result in the healing of cracks and is a viable mechanism for mitigating crack formation.

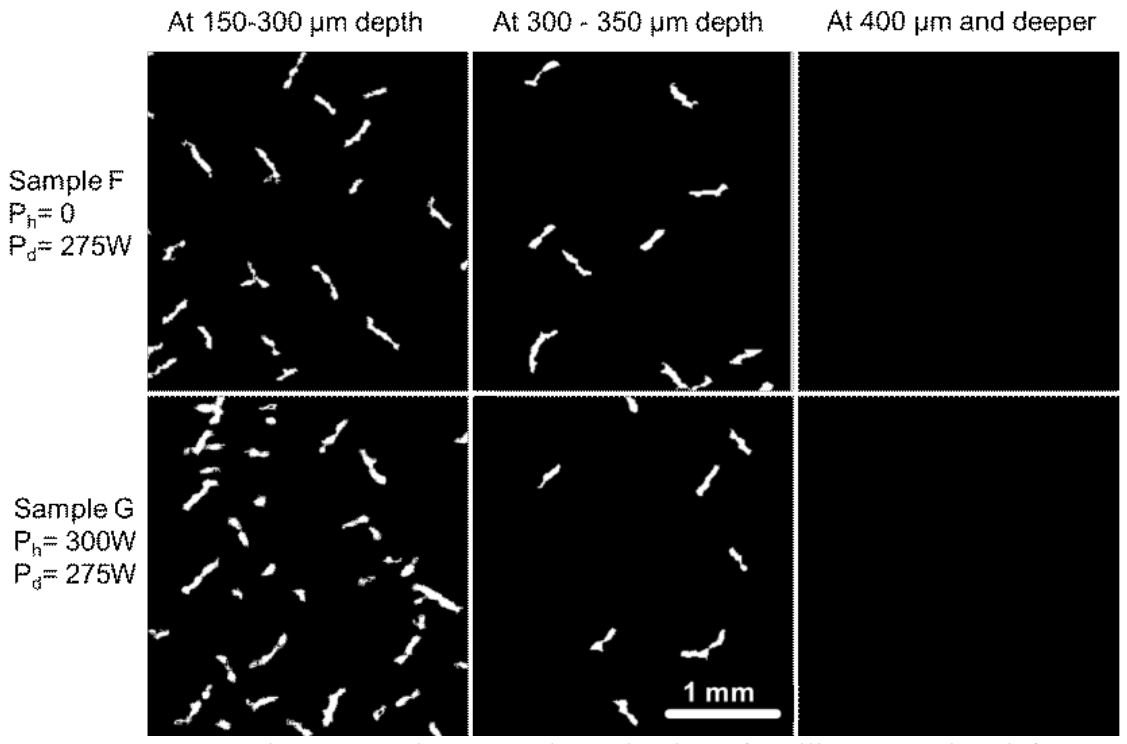


Figure 8: X-ray Computed Tomography (XCT) investigation of Stellite 21 coating defects at different depth measured from the coating surface to the interface region.

3.1.3 Warping

During DED the substrate tends to warp due to the residual thermal stresses. It was observed that warping of the substrate was a function of the laser power and preheat conditions. The procedure used for the measurement of warping is encapsulated in Figure 9(a). The sample tends to warp in a concave up manner. The intent is to ascertain the flatness of the coupon, by averaging the deviation of edges from the ideal plane. From the results depicted in Figure 9 (b) it is observed that the laser power applied during preheating (Ph), and not the deposition power (Pd), has a significant effect on warping. Excessive preheat tends to warp the sample by as much as 0.5 mm. Hence, it is necessary to balance the beneficial effects of preheating in reducing cracking with the deleterious side-effect of warping; the optimal choice identified is sample N.

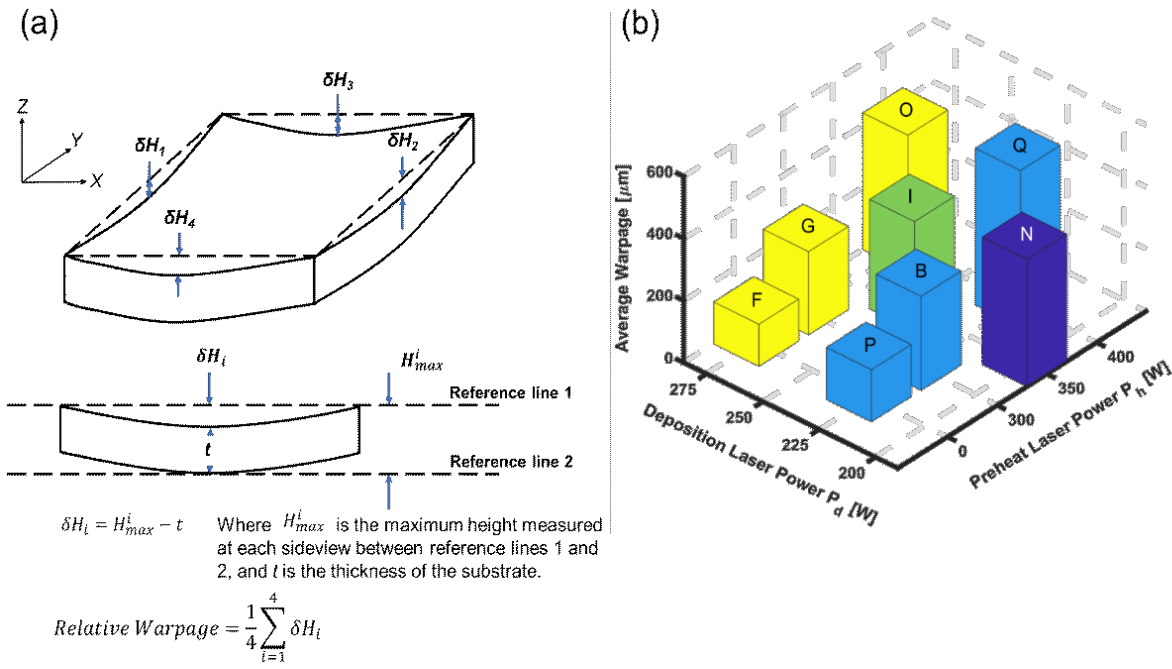


Figure 9: Effect of process parameters on the warping of the substrate: (a) Schematic representation and calculation of the average relative sample warpage; (b) Graphical representation of the average relative warpage as a function of preheating and deposition laser powers.

3.2 Microstructure Characterization

3.2.1 Morphology and composition

The SEM images of the etched and polished sample surfaces are shown in Figure 10. The observation of a dendritic microstructure, contingent on the laser power and preheating conditions in Stellite is consistent with the findings in the literature [5, 21, 22, 26, 31-33]. More pertinently, we observed that cracks occurred without exception along the inter-dendritic regions. The proclivity of the crack formation along the inter-dendritic boundaries is evident in sample P, shown in Figure 10 (bottom left).

To explain the reason for crack formation along the inter-dendritic boundaries, we conducted energy-dispersive X-ray spectroscopy (EDS) point analysis at the representative spots in Figure 10. Spot 1 represents an EDS reading taken at the dendritic region, whilst Spot 2 represents the inter-dendritic region. The EDS analysis, reported in Table 3, shows that in samples with predominant cracking, namely, F, O and P, the difference in the concentration of Cr between dendritic and inter-dendritic regions is consistently higher than that in the nominally crack-free sample (N). A similar trend is evident in Table 3 concerning the concentration of Mo.

In other words, a large difference in Cr and Mo concentrations between the inter-dendritic and dendritic regions are correlated to crack formation. These observations suggest the formation of a brittle Cr-rich carbide phase and Co₃Mo in the inter-dendritic regions, which is susceptible to cracking under thermally-induced stresses [15, 18]. The cracking of Stellite 21 at the inter-dendritic boundaries in Stellite 21 on account of formation of Cr and Mo-rich phases was also observed by Lai *et al.* [34].

Table 3: Elemental concentration in wt.% measurements from the dendritic (Spot 1) and interdendritic (Spot 2) regions. The number in the parenthesis is the standard deviation (n = 4).

	F		0		P		Q		N		
Samples	$P_{d} = 275 \text{ W}$		$P_d = 275 \text{ W}$		$P_d = 225 \text{ W}$		$P_{d} = 225 \text{ W}$		$P_d = 200 W$		
	$P_h = 0 W$	I	$P_{h} = 400$	$P_h = 400 \text{ W}$		$P_h = 0 W$		$P_h = 400 \text{ W}$		$P_h = 350 \text{ W}$	
Elements	Spot 1	Spot 2	Spot 1	Spot 2	Spot 1	Spot 2	Spot 1	Spot 2	Spot 1	Spot 2	
Chromium Content	28.33	30.74	28.17	30.64	28.12	30.29	28.74	30.04	26.9	28.07	
Difference	2.41 (0.8	82)	2.48 (1.	13)	2.17 (0	36)	1.30 (0.	54)	1.18 (0	31)	
Molybdenum Content	1.79	4.94	2.47	5.21	2.68	5.51	2.71	4.52	3.21	4.39	
Difference	3.15 (0.3	57)	2.73 (0.	77)	2.83 (1.	02)	1.82 (0.	08)	1.12 (0.	03)	

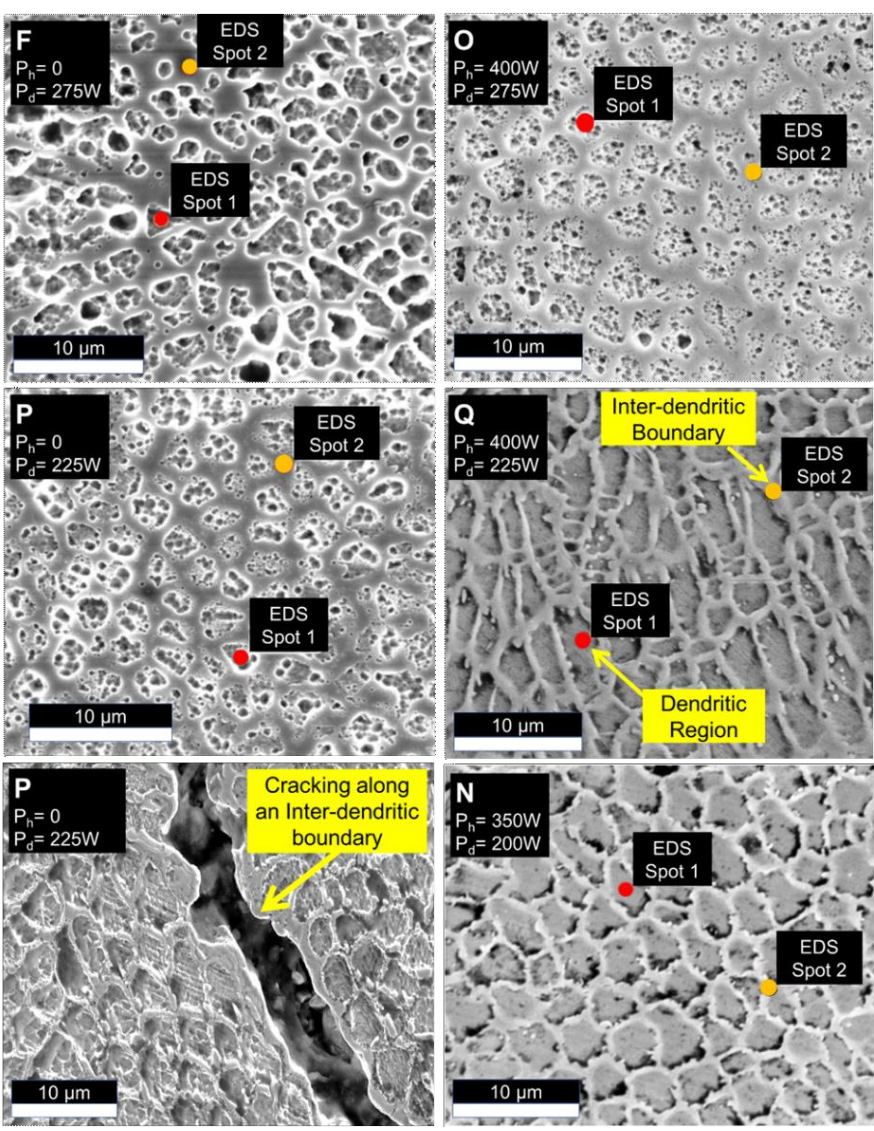


Figure 10: EDS point analysis of polished surfaces of Stellite 21 coating on Inconel 718 alloy under different preheat and deposition power settings, where EDS Spot 1 and Spot 2 represent dendritic and inter-dendritic regions, respectively, and the results are presented in Table 3. The bottom left is an SEM image of cracking along an inter-dendritic boundary in sample P.

3.2.2 Dilution of the Coating

Energy dispersive X-ray Spectroscopy (EDS) elemental line scans were conducted along the transverse cross-sections of three samples (Figure 11). These line scans quantify the effect of process conditions on the dilution of the coating composition due to the diffusion of elements from the substrate. The samples chosen were $P(P_h = 0, P_d = 225 \text{ W})$, $N(P_h = 350 \text{ W}, P_d = 200 \text{ W})$, and $Q(P_h = 400 \text{ W}, P_d = 225 \text{ W})$. These samples were selected because they had less severe cracking compared to samples F and O (Figure 7). Samples F and O were replete with cracks as deep as 350 μ m and therefore deemed infeasible conditions for processing an effective coating.

Figure 11 shows the change in elemental concentration of five alloy constituents, Co, Ni, Fe, Cr, and Mo as a function of distance from the coating surface to the substrate. The greatest change is observed in Co, Ni, and Fe along the EDS line scan; a steep change in elemental composition demarcates the interface between the coating and substrate. The degree of coating dilution by the substrate material is ascertained on comparison of the EDS line scan.

For example, tracking the composition in Samples P and Q revealed that the Cr content ranges from 25% to 30% in the coating region. In contrast in sample N, the Cr content in the coating is in the range of 15% to 20%. Comparing the EDS line scanning for samples P ($P_h = 0$), N ($P_h = 350$ W), and Q ($P_h = 400$ W) in Figure 11(a), (b), and (c), respectively, we observe that the compositional variation along the transverse cross-section of sample Q was less abrupt and occurs over a longer distance (~200 µm) in comparison with sample P. However, the line scan along the transverse cross-section of sample N (moderate preheat, $P_h = 350$ W), shows a steeper compositional variation over a shorter distance (~40 µm) in comparison with sample Q ($P_h = 400$; $P_d = 225$ W).

These changes in the composition in the coating implies that the intermixing between the coating and substrate increases as the preheating power (P_h) increases, consistent with the findings of Zanzarin *et al.* [13]. Another observation is that preheating the substrate prior to the deposition process generates a heat-affected zone (HAZ); the depth of the HAZ increases with the preheat power and promotes the diffusion of alloying elements. The characteristics of the HAZ is discussed in depth in the forthcoming section 3.3.

The variation of the composition over the interface when the preheat power increases is explained as follows. Since the surface of the substrate is melted during preheating, consequently, the high surface temperature of the substrate before deposition of the coating facilitates intermixing and elemental diffusion of the substrate material into the coating. Therefore, the dilution of the coating by the substrate material is exacerbated by an increase in the preheat power (P_h) [13].

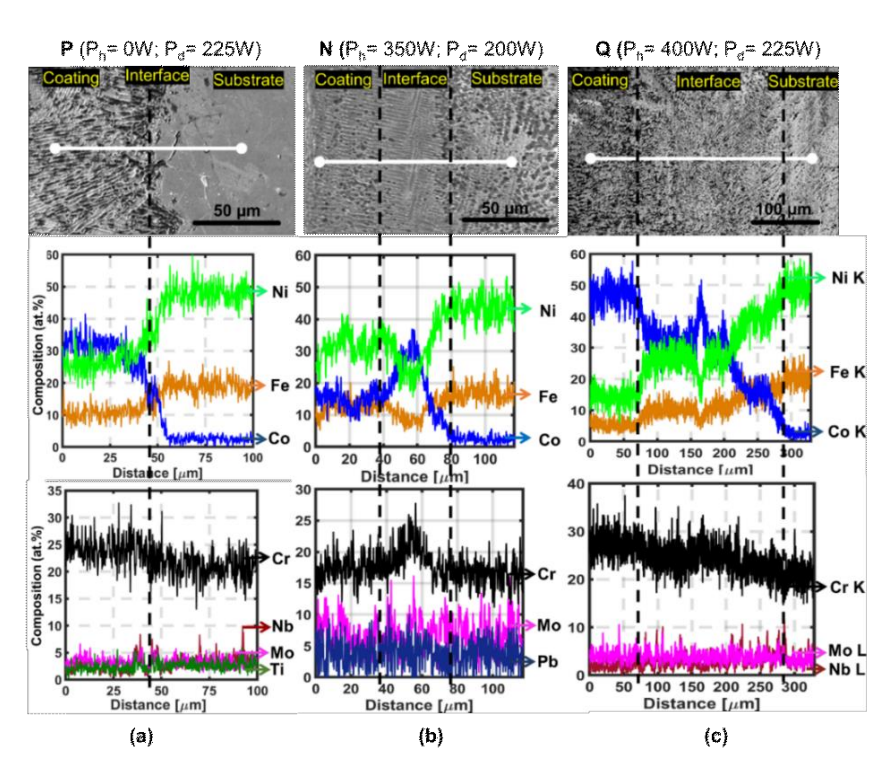


Figure 11: EDS line scan of the transverse cross-section of Stellite 21 coating on Inconel 718 alloy at different preheat conditions (a) Sample P (P_h = 0; P_d = 225 W); (b) Sample N (P_h = 350 W; P_d = 200 W); (c) Sample Q (P_h = 400 W; P_d = 225 W). It is observed that the width of the intermixing region increases as the preheat power (P_h) increases.

3.3 Microhardness

3.3.1 Surface microhardness

The surface microhardness $HV_{0.5}$ of polished and etched samples is reported in Table 4; measurements are taken at six random locations on the surface. The surface microhardness of the Stellite 21 coating, irrespective of the processing condition, was higher than the hardness of the underlying substrate, Inconel 718 alloy, viz., $HV_{0.5} = 320$ (standard deviation, 26). In the literature the higher hardness of the Stellite coating is attributed to the formation of Cr-rich carbides (Cr₇C₃ and Cr₃C₂) and Mo-rich carbide (Co, Mo)₃C in the Co matrix [9, 35-38].

Statistical analysis revealed that the mean value of the surface microhardness for coatings deposited at laser power P_d = 225 W is significantly higher than that for coating deposited at both 275 W and 200 W (5% level of significance). A similar trend in microhardness values with the deposition laser power was also reported by Bartkowski *et. al.*[21]. The lowest mean value of microhardness was observed for sample N, i.e., the nominally crack-free sample. The low hardness of sample N stems from the lower concentration of Cr compared to other samples, as was evident from the EDS point analysis in Table 3. The reduced Cr concentration decreases the brittleness (at the cost of hardness), and consequently mitigates crack formation due to thermally-induced stresses.

Table 4: Microhardness measurements ($HV_{0.5}$) of polished surfaces of Stellite 21 coatings deposited under different conditions of preheating (P_h) and deposition power (P_d) in Watts.

Sample	HV _{0.5} mean (standard deviation, n =6)
$F(P_h = 0, P_d = 275)$	379 (9)
$O(P_h = 400, P_d = 275)$	389 (12)
$P(P_h = 0, P_d = 225)$	400 (12)
$Q(P_h = 400, P_d = 225)$	399 (22)
$N (P_h = 350, P_d = 200)$	366 (11)

3.3.2 Microhardness across the cross-section of the coating

Figure 12 shows the transverse cross-section microstructure and microhardness profiles for samples F, O, P, and Q. The microhardness in Figure 12 (c) and (d) is measured at five random locations at a particular depth. The microhardness readings correspond to their respective micrographs in Figure 12 (a), (b), (e) and (f); the error bars are one standard deviation wide. Likewise, the microhardness for the nominally crack-free Sample N as a function of its microstructure is characterized in Figure 13. The decreasing trend in the microhardness observed in Figure 12 and Figure 13 with the distance from the coating surface is consistent with previous studies on Co-based coatings[10, 21, 28, 39-42]; the decrease in hardness is attributed to the change in the microstructure, dilution of the coating composition, and poor material consolidation.

Accordingly, referring to Figure 12 and Figure 13, the microhardness profile along the cross-section can be demarcated into four regions: (i) the surface coating region, which has the highest hardness; (ii) the intermixing region which has a reduced hardness due to diffusion of Fe and Ni into the coating from the substrate; (iii) the heat-affected zone; and (iv) the substrate. The surface coating region, referring to Figure 13, extends to a depth $\approx 100~\mu m$ from the surface (after polishing), and has a finer dendritic microstructure relative to the other three regions of the coating. Consistent with the hardness recorded on the surface (Table 4), the hardness of the coating region is a function of the deposition power; the maximum hardness value was achieved at a moderate deposition power ($P_d = 225~W$) and not at the high deposition power ($P_d = 275$).

The surface coating region is followed by an intermixed region where the hardness values tend to decrease precipitously due to dilution of the coating composition with Fe and Ni from the substrate. Next is the heat-affected zone (HAZ), whose depth is proportional to the deposition laser power (P_d) and preheat power (P_h). The effect of preheating the substrate on the depth of the HAZ

is estimated from Figure 12 and Figure 13 based on visual inspection of the microstructure. The microstructure of the HAZ is finer than that of the unaffected substrate, and it has a higher hardness due to remelting and rapid solidification. For example, from Figure 12(a) and (b) for sample O and Q, respectively, with $P_h = 400$ W the depth of the HAZ ~330 μ m. Likewise, in Figure 13(a) for sample N (P_h =350 W), the HAZ is approximately 280 μ m deep. In comparison, for sample F and P deposited at $P_h = 0$ W in Figure 12(e) and (f), the HAZ has a thickness of 25 μ m to 50 μ m.

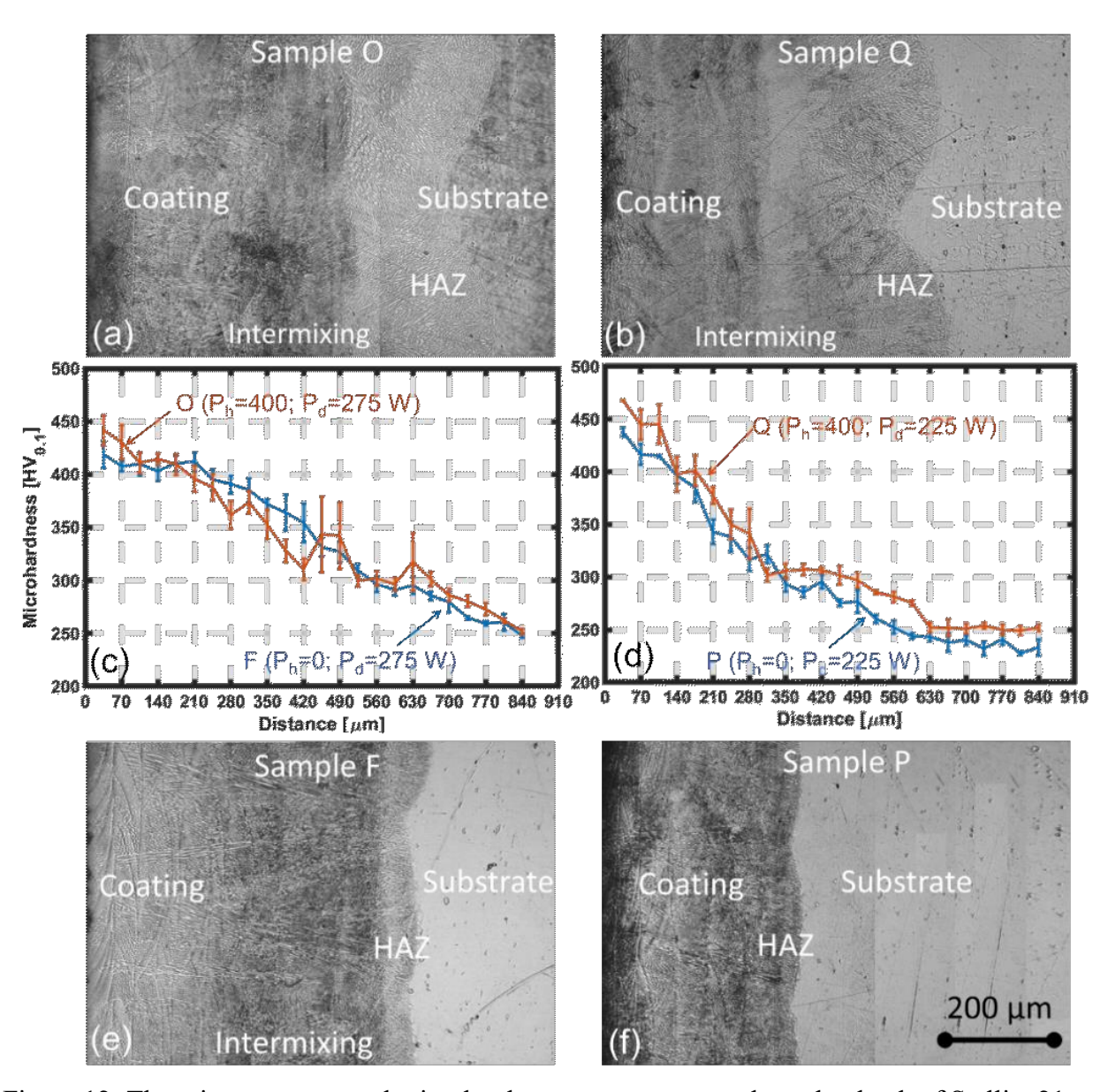


Figure 12: The microstructure and microhardness measurements along the depth of Stellite 21 coating deposited on Inconel 718 under different preheat and deposition laser powers.

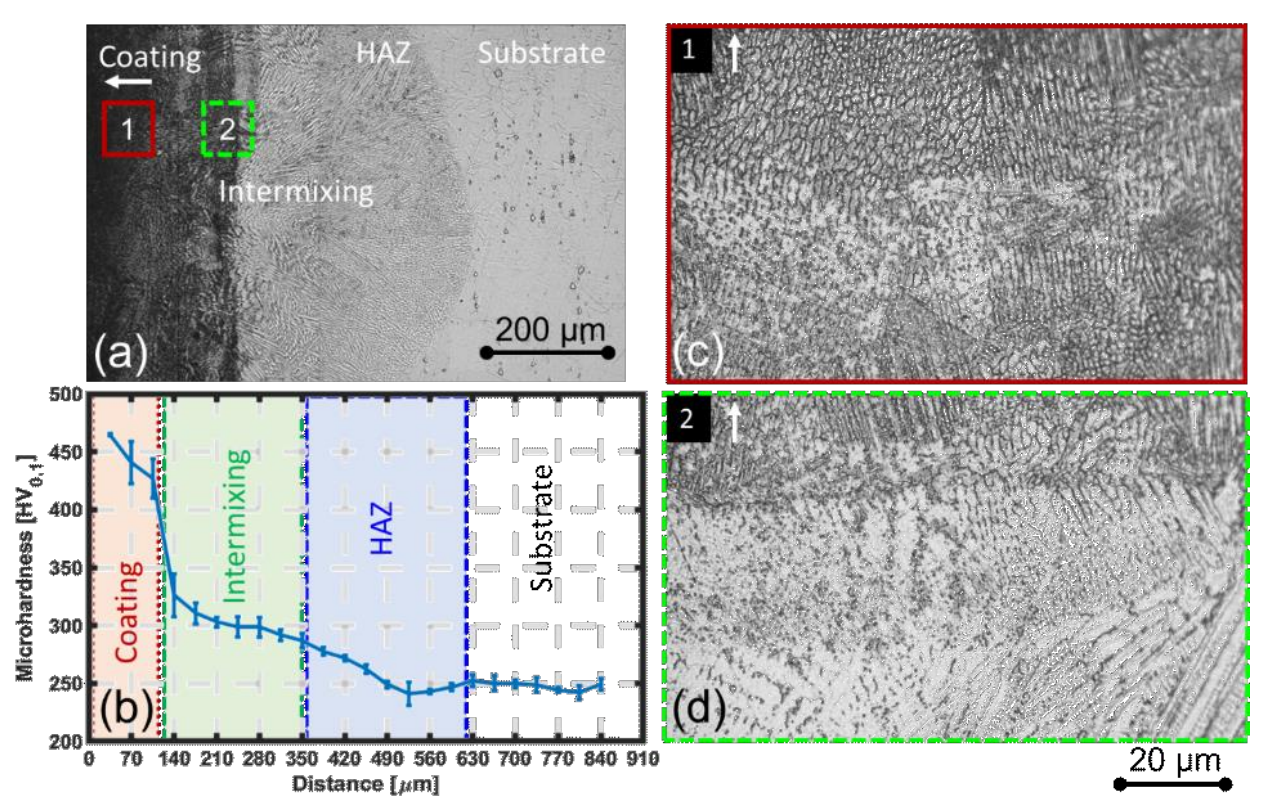


Figure 13: (a) Cross-section of Sample (N), (b) microhardness measurements along the depth of sample N corresponding to the cross-section in (a) above, (c) and (d) optical images of two locations marked 1 and 2, respectively in (a). The arrow indicates the direction of the top surface of the coating.

3.4 Correlation of in-process temperature data to crack formation

In this section, we acquire in-situ temperature measurements to substantiate that the cracking is linked to the thermal history of the part during deposition, which in turn is a function of the input energy density. We show that cracking is mitigated by minimizing steep temperature gradients, through a pragmatic choice of laser power and preheating. In Figure 14, we compare the temperature trends for the five samples, F, O, P, Q, and N measured by a thermocouple in contact with the substrate (*Far TC* shown in Figure 2(b)). Data from all the three thermocouples used in this work show similar trends in the part temperature, hence we only show data from *Far TC*.

There is a gradual increase in temperature as scanning starts from the side of the coupon furthest from the thermocouple. The cyclical nature of the temperature trace observed at this fixed

measurement point is the salient aspect of these plots. The spikes in the plot correspond to the 12 deposited layers and the two preheating passes where applicable (demarcated as h1 and h2, in samples O, Q, N).

Table 5 summarizes in-process thermal data observed from temperature graphs illustrated in Figure 14 in terms of the average peak-to-valley temperature along with the standard deviation over 12 layers. The first pertinent observation from Figure 14(a) is that the samples with predominant cracking (sample F and O, $P_d = 275$ W) have the highest average peak-to-valley amplitude of nearly 30 °C, as well as large variability (standard deviation, ~ 3.5 °C). When the laser power is reduced from 275 W (Figure 14 (a)) to 225 W (Figure 14(b)) for samples P and Q ($P_d = 225$ W), the amplitude drops by nearly 18% for samples deposited without preheating and more than 45% for samples deposited with preheating the substrate.

Further evident in Figure 14(b) is the beneficial effect of preheating in reducing steep thermal gradients. The temperature during the deposition of Sample Q (P_d = 225 W, P_h =400 W) is consistent between 130 °C and 150 °C, and the average peak-to-valley temperature amplitude is close to 17 °C. In comparison with Sample Q, the peak temperature profile for Sample P (P_d = 225 W, P_h = 0 W) shows a steady increase from 50 °C from layer 1 to 150 °C at layer 12, with the peak-to-valley temperature amplitude as large as 28 °C.

To further accentuate the contrasting effect of laser power and preheating, in Figure 14 (c) the sample with the highest crack density (sample F) is compared with the nominally crack-free sample (sample N). In the case of sample N, the peak-to-valley amplitude temperature difference is largely steady from the start of deposition to the end of deposition and is only \sim 18 °C with a standard deviation of less than 1 °C. In contrast, the temperature gradually rises for sample F

(which is not preheated), and the peak-to-valley temperature difference reaches nearly (40 °C) towards the end of the deposition.

The in-situ temperature profiles confirm that the large variation in temperature across the entire deposition process, and between the start and end of a layer in samples processed without preheating and at high deposition power, (e.g., sample F) is the main cause of cracking. Preheating arrests the continual rise in temperature across the whole of the deposition process, and a moderate deposition power prevents a large variation in temperature between layers.

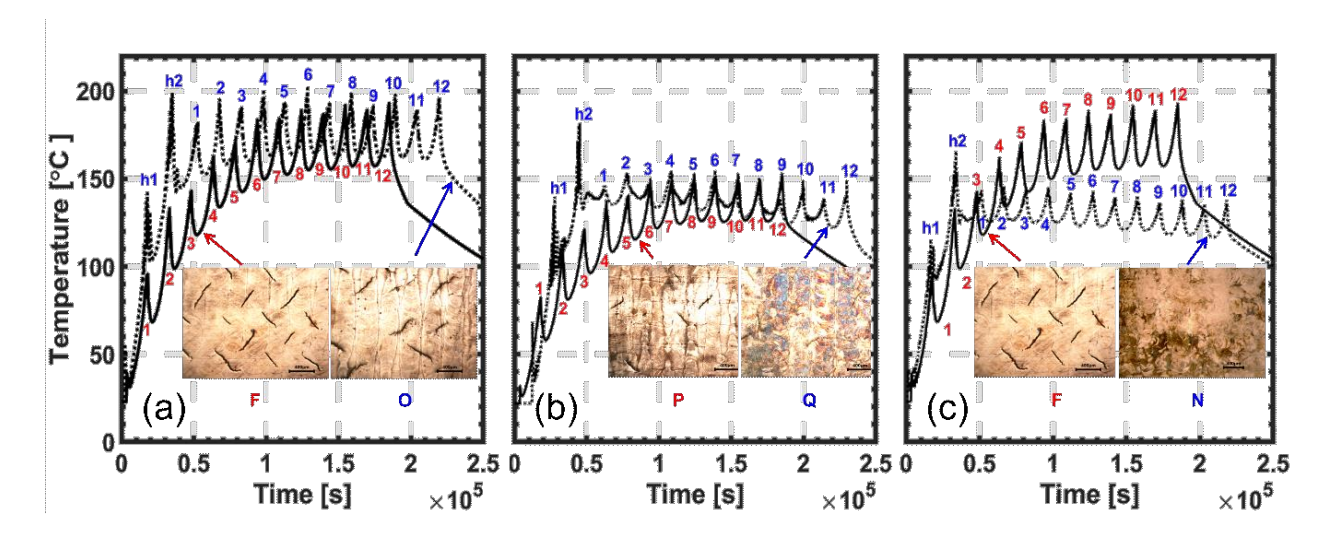


Figure 14: Thermal phenomena acquired during preheat and deposition process for samples (a) F ($P_h=0$ W; $P_d=275$ W) versus O ($P_h=400$ W; $P_d=275$ W), (b) P ($P_h=0$ W; $P_d=225$ W) versus Q ($P_h=400$ W; $P_d=225$ W), and (c) F ($P_h=400$ W; $P_d=275$ W) versus N ($P_h=350$ W; $P_d=200$ W).

Table 5: Average peak-to-valley temperature for the five selected samples. The number in the parenthesis is the standard deviation over the 12 layers.

Sample	Processing Condition	Average Peak-to-valley temperature [°C] (std. deviation)
F	$P_h = 0 \text{ W}, P_d = 275 \text{ W}$	31.3 (3.33)
0	$P_h = 400 \text{ W}, P_d = 275 \text{ W}$	32.5 (3.43)
P	$P_h = 0 \text{ W}, P_d = 225 \text{ W}$	25.5 (2.06)
Q	$P_h = 400 \text{ W}, P_d = 225 \text{ W}$	17.6 (4.36)
\mathbf{N}	$P_h = 350 \text{ W}, Pd = 200 \text{ W}$	18.7 (0.91)

4 Conclusions

This work investigates the effect of processing conditions, namely laser power and preheating on the characteristics – crack formation, microstructural evolution, dilution and the microhardness of the coating – of Stellite 21 coatings deposited on Inconel 718 substrates using the DED process. Specific conclusions are summarized hereunder.

Cracking of DED-processed Stellite 21 coatings is observed exclusively along the interdendritic boundaries. The coating cracks when inter-dendritic regions, which are rich in brittle Cr and Mo phases, are exposed to high thermally induced residual stresses. Furthermore, cracks were only restricted to the topmost layers and no cracks were observed at the coating-substrate interface.

Cracking of Stellite coatings was mitigated by preheating the substrate and regulating the energy density for deposition to a moderate level. Localized preheating of the substrate with the laser leads to a stable temperature trend over the entire deposition process, and moderate to low deposition power reduces the variation in temperature between layers. The reduction of temperature variation arrests thermally induced residual stresses and segregation of Cr and Mo to the inter-dendritic boundaries.

The laser power used for deposition and preheating influences the microstructure characteristics, chemistry (dilution), and properties of the coating. Excessive preheating of the substrate increases the depth of the heat-affected zone, sample warpage, and dilution of the coating with the substrate material, mainly Ni and Fe, which decreases its hardness. Microhardness profiles showed that the hardness is significantly higher at moderate deposition laser power and the hardness increases with the distance from the interface to the coating surface.

Crack-free coatings are obtained at a volumetric energy density $E_v = P_d/(V \cdot T \cdot H) = 200$ [J·mm⁻³]. In the context of this work, the recommended process window translates to: deposition power $P_d = 200$ W and preheat $P_h = 350$ W; velocity V = 10.6 mm·s⁻¹; layer height T = 0.25 mm; and hatch spacing H = 0.375 mm.

Acknowledgements

The research was performed in part in the Nebraska Nanoscale Facility: National Nanotechnology Coordinated Infrastructure under award no. ECCS: 1542182, and with support from the Nebraska Research Initiative through the Nebraska Center for Materials and Nanoscience and the Nanoengineering Research Core Facility at the University of Nebraska-Lincoln. Prahalada Rao thanks the National Science Foundation (NSF) for funding this work under award CMMI 1752069.

Data Availability

The data required to reproduce these findings can be shared on request.

References

- [1] Crook, P., 1990, "Cobalt and cobalt alloys," ASM International, Metals Handbook, Tenth Edition., 2, pp. 446-454
- [2] de Rosset, W. S., and Montgomery, J. S., 2014, "Cobalt-base alloy gun barrel study," Wear, 316(1), pp. 119-123.doi:https://doi.org/10.1016/j.wear.2014.05.001
- [3] Yao, M. X., Wu, J. B. C., and Xie, Y., 2005, "Wear, corrosion and cracking resistance of some W- or Mo-containing Stellite hardfacing alloys," Materials Science and Engineering: A, 407(1), pp. 234-244.doi:https://doi.org/10.1016/j.msea.2005.06.062
- [4] Clare, A. T., Oyelola, O., Abioye, T. E., and Farayibi, P. K., 2013, "Laser cladding of rail steel with Co–Cr," Surface Engineering, 29(10), pp. 731-736.doi:10.1179/1743294412Y.0000000075
- [5] Traxel, K. D., and Bandyopadhyay, A., 2019, "First Demonstration of Additive Manufacturing of Cutting Tools using Directed Energy Deposition System: StelliteTM-Based Cutting Tools," Additive Manufacturing, 25, pp. 460-468.doi:https://doi.org/10.1016/j.addma.2018.11.019
- [6] Bartkowski, D., and Bartkowska, A., 2017, "Wear resistance in the soil of Stellite-6/WC coatings produced using laser cladding method," International Journal of Refractory Metals and Hard Materials, 64, pp. 20-26.doi:https://doi.org/10.1016/j.ijrmhm.2016.12.013
- [7] Foster, J., Cullen, C., Fitzpatrick, S., Payne, G., Hall, L., and Marashi, J., 2019, "Remanufacture of hot forging tools and dies using laser metal deposition with powder and a hard-facing alloy Stellite 21®," Journal of Remanufacturing, 9(3), pp. 189-203.doi:10.1007/s13243-018-0063-9
- [8] Gibson, I., Rosen, D. W., and Stucker, B., 2014, Additive manufacturing technologies, Springer.
- [9] Atamert, S., and Bhadeshia, H. K. D. H., 1989, "Comparison of the microstructures and abrasive wear properties of stellite hardfacing alloys deposited by arc welding and laser cladding," Metallurgical Transactions A, 20(6), pp. 1037-1054.doi:10.1007/bf02650140
- [10] Kathuria, Y. P., 2000, "Some aspects of laser surface cladding in the turbine industry," Surface and Coatings Technology, 132(2), pp. 262-269.doi:https://doi.org/10.1016/S0257-8972(00)00735-0
- [11] Xu, G., Kutsuna, M., Liu, Z., and Yamada, K., 2006, "Comparison between diode laser and TIG cladding of Co-based alloys on the SUS403 stainless steel," Surface and Coatings Technology, 201(3), pp. 1138-1144.doi:https://doi.org/10.1016/j.surfcoat.2006.01.040
- [12] Tiziani, A., Giordano, L., Matteazzi, P., and Badan, B., 1987, "Laser stellite coatings on austenitic stainless steels," Materials Science and Engineering, 88, pp. 171-175.doi: https://doi.org/10.1016/0025-5416(87)90082-6
- [13] Zanzarin, S., Bengtsson, S., and Molinari, A., 2015, "Study of carbide dissolution into the matrix during laser cladding of carbon steel plate with tungsten carbides-stellite powders," Journal of Laser Applications, 27(S2), p. S29209.doi:10.2351/1.4906480

- [14] Jendrzejewski, R., Śliwiński, G., Krawczuk, M., and Ostachowicz, W., 2004, "Temperature and stress fields induced during laser cladding," Computers & Structures, 82(7), pp. 653-658.doi:https://doi.org/10.1016/j.compstruc.2003.11.005
- [15] Ganesh, P., Moitra, A., Tiwari, P., Sathyanarayanan, S., Kumar, H., Rai, S. K., Kaul, R., Paul, C. P., Prasad, R. C., and Kukreja, L. M., 2010, "Fracture behavior of laser-clad joint of Stellite 21 on AISI 316L stainless steel," Materials Science and Engineering: A, 527(16), pp. 3748-3756.doi:https://doi.org/10.1016/j.msea.2010.03.017
- [16] Liu, R., Xi, S., Kapoor, S., and Wu, X., 2010, "Effects of chemical composition on solidification, microstructure and hardness of Co-Cr-W-Ni and Co-Cr-Mo-Ni alloy systems," Int J Res Rev Appl Sci, 5, pp. 110-122
- [17] Liu, R., Yao, J., Zhang, Q., Yao, M. X., and Collier, R., 2015, "Effects of molybdenum content on the wear/erosion and corrosion performance of low-carbon Stellite alloys," Materials & Design, 78, pp. 95-106.doi:https://doi.org/10.1016/j.matdes.2015.04.030
- [18] Huang, P., Liu, R., Wu, X., and Yao, M. X., 2006, "Effects of Molybdenum Content and Heat Treatment on Mechanical and Tribological Properties of a Low-Carbon Stellite® Alloy," Journal of Engineering Materials and Technology, 129(4), pp. 523-529.doi:10.1115/1.2744429
- [19] Liu, R., Yao, M., Patnaik, P., and Wu, X., 2006, "An improved wear-resistant PTA hardfacing: VWC/Stellite 21," Journal of composite materials, 40(24), pp. 2203-2215
- [20] Díaz, E., Amado, J., Montero, J., Tobar, M., and Yáñez, A., 2012, "Comparative study of Co-based alloys in repairing low Cr-Mo steel components by laser cladding," Physics Procedia, 39, pp. 368-375
- [21] Bartkowski, D., Młynarczak, A., Piasecki, A., Dudziak, B., Gościański, M., and Bartkowska, A., 2015, "Microstructure, microhardness and corrosion resistance of Stellite-6 coatings reinforced with WC particles using laser cladding," Optics & Laser Technology, 68, pp. 191-201.doi:https://doi.org/10.1016/j.optlastec.2014.12.005
- [22] D'Oliveira, A. S. C. M., da Silva, P. S. C. P., and Vilar, R. M. C., 2002, "Microstructural features of consecutive layers of Stellite 6 deposited by laser cladding," Surface and Coatings Technology, 153(2), pp. 203-209.doi:https://doi.org/10.1016/S0257-8972(01)01687-5
- [23] Jendrzejewski, R., Navas, C., Conde, A., de Damborenea, J. J., and Śliwiński, G., 2008, "Properties of laser-cladded stellite coatings prepared on preheated chromium steel," Materials & Design, 29(1), pp. 187-192.doi:https://doi.org/10.1016/j.matdes.2006.10.020
- [24] Fallah, V., Alimardani, M., Corbin, S. F., and Khajepour, A., 2010, "Impact of localized surface preheating on the microstructure and crack formation in laser direct deposition of Stellite 1 on AISI 4340 steel," Applied Surface Science, 257(5), pp. 1716-1723.doi:https://doi.org/10.1016/j.apsusc.2010.09.003
- [25] Brueckner, F., Lepski, D., Nowotny, S., Leyens, C., and Beyer, E., 2012, "Calculating the stress of multi-track formations in induction-assisted laser cladding," International Congress on Applications of Lasers & Electro-Optics, pp. 176-182
- [26] Alimardani, M., Fallah, V., Khajepour, A., and Toyserkani, E., 2010, "The effect of localized dynamic surface preheating in laser cladding of Stellite 1," Surface and Coatings Technology, 204(23), pp. 3911-3919.doi:https://doi.org/10.1016/j.surfcoat.2010.05.009

- [27] Davis, J. R., 2000, Nickel, cobalt, and their alloys, ASM international, Materials Park, OH.
- [28] Singh, R., Kumar, D., Mishra, S. K., and Tiwari, S. K., 2014, "Laser cladding of Stellite 6 on stainless steel to enhance solid particle erosion and cavitation resistance," Surface and Coatings Technology, 251, pp. 87-97.doi:https://doi.org/10.1016/j.surfcoat.2014.04.008
- [29] Budiansky, B., and O'Connell, R. J., 1976, "Elastic moduli of a cracked solid," International Journal of Solids and Structures, 12(2), pp. 81-97.doi:https://doi.org/10.1016/0020-7683(76)90044-5
- [30] Sun, S., Durandet, Y., and Brandt, M., 2005, "Parametric investigation of pulsed Nd: YAG laser cladding of stellite 6 on stainless steel," Surface and Coatings Technology, 194(2), pp. 225-231.doi:https://doi.org/10.1016/j.surfcoat.2004.03.058
- [31] Hidouci, A., Pelletier, J. M., Ducoin, F., Dezert, D., and El Guerjouma, R., 2000, "Microstructural and mechanical characteristics of laser coatings," Surface and Coatings Technology, 123(1), pp. 17-23.doi:https://doi.org/10.1016/S0257-8972(99)00394-1
- [32] Bartkowski, D., and Kinal, G., 2016, "Microstructure and wear resistance of Stellite-6/WC MMC coatings produced by laser cladding using Yb:YAG disk laser," International Journal of Refractory Metals and Hard Materials, 58, pp. 157-164.doi:https://doi.org/10.1016/j.ijrmhm.2016.04.017
- [33] Cui, C., Guo, Z., Liu, Y., Xie, Q., Wang, Z., Hu, J., and Yao, Y., 2007, "Characteristics of cobalt-based alloy coating on tool steel prepared by powder feeding laser cladding," Optics & Laser Technology, 39(8), pp. 1544-1550.doi:https://doi.org/10.1016/j.optlastec.2006.12.005
- [34] Lai, Q., Abrahams, R., Yan, W., Qiu, C., Mutton, P., Paradowska, A., Soodi, M., and Wu, X., 2019, "Influences of depositing materials, processing parameters and heating conditions on material characteristics of laser-cladded hypereutectoid rails," Journal of Materials Processing Technology, 263, pp. 1-20.doi:https://doi.org/10.1016/j.jmatprotec.2018.07.035
- [35] Antony, K. C., 1983, "Wear-Resistant Cobalt-Base Alloys," JOM, 35(2), pp. 52-60.doi:10.1007/bf03338205
- [36] Liu, R., Yao, J. H., Zhang, Q. L., Yao, M. X., and Collier, R., 2015, "Microstructures and Hardness/Wear Performance of High-Carbon Stellite Alloys Containing Molybdenum," Metallurgical and Materials Transactions A, 46(12), pp. 5504-5513.doi:10.1007/s11661-015-3132-9
- [37] Liu, R., Yao, J. H., Zhang, Q. L., Yao, M. X., and Collier, R., 2015, "Relations of Chemical Composition to Solidification Behavior and Associated Microstructure of Stellite Alloys," Metallography, Microstructure, and Analysis, 4(3), pp. 146-157.doi:10.1007/s13632-015-0196-2
- [38] Kapoor, S., 2012, "High-temperature hardness and wear resistance of stellite alloys," MS Thesis, Carleton University, Ottawa, Ontario, Canada.
- [39] Farnia, A., Malek Ghaini, F., Ocelík, V., and De Hosson, J. T. M., 2013, "Microstructural characterization of Co-based coating deposited by low power pulse laser cladding," Journal of Materials Science, 48(6), pp. 2714-2723.doi:10.1007/s10853-012-7069-8
- [40] Gholipour, A., Shamanian, M., and Ashrafizadeh, F., 2011, "Microstructure and wear behavior of stellite 6 cladding on 17-4 PH stainless steel," Journal of Alloys and Compounds, 509(14), pp. 4905-4909.doi:https://doi.org/10.1016/j.jallcom.2010.09.216

- [41] Sidhu, T. S., Prakash, S., and Agrawal, R. D., 2006, "Studies of the metallurgical and mechanical properties of high velocity oxy-fuel sprayed stellite-6 coatings on Ni- and Fe-based superalloys," Surface and Coatings Technology, 201(1), pp. 273-281.doi:https://doi.org/10.1016/j.surfcoat.2005.11.108
- [42] Niederhauser, S., and Karlsson, B., 2003, "Mechanical properties of laser cladded steel," Materials Science and Technology, 19(11), pp. 1611-1616.doi:10.1179/026708303225008103